



Mueller matrix study of the dichroism in nanorods dimers: rod separation effects

CAROLINA DE DIOS, ALBA JIMÉNEZ, FERNANDO GARCÍA, ANTONIO GARCÍA-MARTÍN, ALFONSO CEBOLLADA, AND GASPAR ARMELLES*

IMN-Instituto de Micro y Nanotecnología de Madrid (CNM-CSIC), Isaac Newton 8, PTM, Tres Cantos, E-28760 Madrid, Spain

**gaspar.armelles@csic.es*

Abstract: We have studied the optical response of chiral metastructures composed of a disordered array of couples of plasmonic Au nanorods helically piled along the vertical direction. The fabrication is based on the use of multiaxial and multimaterial evaporation of the different metastructure building blocks through nanohole masks. From the analysis of the Mueller Matrix elements of the system, obtained both experimentally and from dedicated numerical simulations in forward and backward illumination conditions, we have been able to determine the linear and circular dichroic response of the system, as well as to sort out the optical anisotropy and intrinsic circular dichroism contributions to the circular differential extinction. We have also analyzed the dependence of the optical properties as a function of the angle between the rods and of the thickness of the dielectric separator. The study of quasi-planar as well as three-dimensional structures allows unraveling the role played by interactions between the constituting building blocks and, in particular, the distance between rods. We have experimentally and theoretically observed a decrease of the circular dichroic contribution and a change of the optical anisotropic contribution when the structures evolve from non-planar to planar.

© 2019 Optical Society of America under the terms of the [OSA Open Access Publishing Agreement](#)

1. Introduction

Metastructures with tailored optical response can be obtained by smart spatial combination of different, simple building blocks exhibiting well-known optical properties. The individual properties and the specific spatial localization, either in two- or three-dimensions, allow obtaining complex systems with properties, ruled now via interactions, not achievable otherwise. A versatile plasmonic building block is the metallic rod, whose plasmonic resonances can be spectrally tuned by material and dimensions choice. Besides, they respond differently to light polarized along the principal axes of the rod [1,2]. Actually, this asymmetry in the optical response lies behind the development of different types of polarization-sensitive devices. When arranging rods in a 2D or 3D fashion, the electromagnetic interaction between them induces new optical properties [3–6]. For example, structures with linear and circular dichroism can be obtained just by combining different in-plane inter rod orientations with a smart piling up of them. The simplest example is vertically stacking two rods with their long axes twisted with respect to each other, making rods dimers good candidates for chiral sensing applications [7].

The fabrication of these 3D stacked rod dimers can be approached in different ways. For example using multistep lithographic (electron beam lithography and vacuum deposition techniques) or chemical routes. Using multistep electron beam lithography and vacuum deposition, dimers with inter rods distance of more than 40 nm and with variable relative orientation between the rods have been fabricated [8–11]. Alternatively, using chemical routes, dimers with inter rod distances of only a few nanometers, but with a much less accurate control of the relative orientation between the rods, have also been obtained [12–16].

In this work we study the linear and circular dichroic responses as well as the role of inter-rod interactions in 3D chiral Au nanorod dimers. From the fabrication point of view, we make use of a well-known shadow nanomask evaporation technique [17], in our case with different materials to evaporate in the deposition system, and polar and azimuthal degrees of freedom in the relative orientation of the nanomask-substrate unit with respect to the incoming beam of material. This has allowed us to obtain, in single deposition runs, a large variety of disordered arrays of 2D and pseudo 3D nanostructures with different shapes and components (disks [18–22], rods [2], complex rings [23–26]). In the present work, this has allowed us to achieve a fine control of the inter-rod relative orientation, but also to tune the vertical separation between them at the nanometer level. In this way, we have ample freedom to tune the interaction between the rods and, therefore, their optical characteristics. In particular, we focus on the different response to linear and circular polarized light, clarifying the different contributions to these signals. To complete the analysis of this optical response we show complementary experimental and theoretical results, where we make use of the Mueller matrix formalism, in forward and backward illumination conditions, as it is the most convenient procedure, to obtain a detailed description of the optical response of systems with a high degree of geometrical complexity.

2. Fabrication

The model structure considered for the rod dimers and generated under each nanohole of the mask is as follows: first a bottom Au rod with two adjacent CaF_2 pillars is deposited on BK7 substrates (previous deposition of Ti insures adhesion of the complete structure). Then, a CaF_2 rod is deposited along the line intersecting the pillars and the central part of the bottom rod. Finally, an upper Au rod is deposited on top of the CaF_2 rod. Mild sonication in adequate solvents favors the removal of the polymer nanomask, leaving the BK7 substrates with a disordered array of rod dimers. This way both Au rods are vertically separated by a distance that is controlled by the thickness of the dielectric, CaF_2 , rod, presenting a twisting angle that can be varied at will. CaF_2 and Ti are deposited by electron beam evaporation, while Au is evaporated from an effusion cell. In Fig. 1 we present a sequential sketch of the multiaxial deposition process, described in detail elsewhere [24].

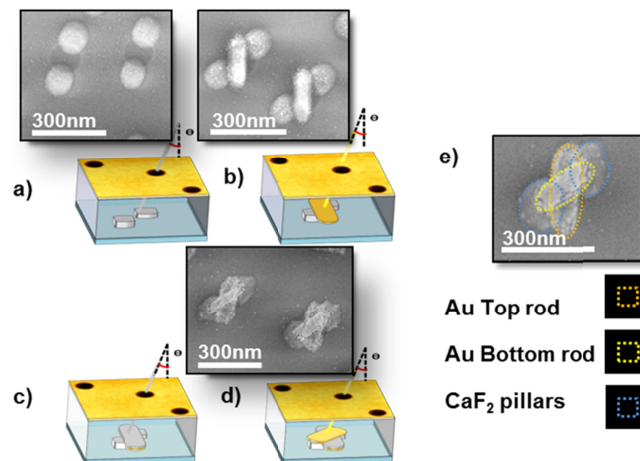


Fig. 1. Scheme representing the fabrication process of the chiral metasurface by a combination of shadow nanomask evaporation technique and multiaxial evaporation: (a) Initially, two pillars of CaF_2 are fabricated through the holes of the gold mask. The dimensions and the distance between the pillars are controlled by the evaporation system. (b) The gold bottom rod is manufactured between the pillars of CaF_2 (c) A dielectric spacer is placed on the bottom rod. (d) The fabrication process is finished by rotating the structure 45° and evaporating a gold rod on the dielectric spacer and the dielectric pillars. To explain the process, SEM images of

intermediate samples are included. (e) SEM image of the chiral metasurface with top rod at 45° obtained in this way.

Despite its versatility, the described fabrication method presents some intrinsic shortcomings that condition the actual choice on dimensions for the different elements, and on whose existence one must be aware. One of the drawbacks is the limitation in controlling of the spatial arrangement of the structures. Although it is possible to precisely stack the structures, the planar spacing is difficult to manage. The most relevant disadvantage is the gradual reduction of the diameter of the nanoholes in the mask, due to the accumulated material during deposition at oblique incidence [27]. As a consequence, the final elements in the metastructure are narrower and, for the same substrate oscillation span, shorter. This gradual hole diameter reduction also limits the total amount of deposited material and consequently the total height of the metastructure. As a consequence, the typical dimensions when the deposited heights of the different elements of the metastructure are 12nm Au/6nm CaF₂/12nm Au/3 nm Ti/0.5mm BK7 result to be: (i) widths and lengths are 95 nm and 235 nm for the bottom rod and are 75 nm and 220 nm for the top rod, (ii) diameters of 20nm thick CaF₂ pillars are 135nm and 100nm, respectively.

3. Results and discussion

The optical properties of the samples have been studied using a spectroscopic ellipsometer (SE, M200Fi J. A. WoollamCo.) in transmission mode at normal incidence in the 400-1600 nm spectral range. In spectroscopic ellipsometers with PCSA configuration of the optical elements (polarizer, compensator, sample and analyzer), the elements of row 4 of the Mueller matrix (m_{41} , m_{42} , m_{43} and m_{44}) cannot be obtained due to the lack of a second compensator [28]. From symmetry considerations, we have used a valid method based on measurements with sample illumination from the metastructures side (Front-F) or from the substrate side (Back-B) [29,30]. This allows, for example, to discern the different contributions of the system to the circular differential extinction [26,31]. The sample was mounted on a rotational stage which allows changing the in-plane orientation of the sample. Following this procedure it is possible to obtain the Mueller Matrix Elements (MME) of the system [28,32], containing full information about different optical aspects of the system [33,34]. As schematically indicated in the left of Fig. 2, in transmission mode, the element m_{12} is directly related to the absorption difference for light that is polarized parallel or perpendicular to the x-axis ($m_{12} = (I_x - I_y)/2$, linear dichroism (LD)). On the other hand, m_{13} is related to the difference in the absorption of light polarized parallel and perpendicular to an axis rotated 45 degrees with respect to the x-axis, x' -axis, ($m_{13} = (I_{x'} - I_{y'})/2$, linear dichroism at 45° (LD')). Finally, m_{14} is related to the difference in transmission for left- and right-handed circularly polarized light ($m_{14} = (I_R - I_L)/2$ or circular differential extinction (CDE)). The measured MME are normalized to the element m_{11} , which is the total transmission intensity of the sample [28]. In Fig. 2 we show the measured MME for three fabricated structures, namely single Au nanorods with CaF₂ pillars symmetrically positioned at both sides of the rods, and complete Au rod dimers at 45° and -45° degrees respectively with 6 nm thick CaF₂ dielectric rods separating them. SEM images for individual structures are also shown. For the experimental determination of the MME, the samples were carefully aligned in the plane so that the long axes of the Au rods close to the substrate were oriented along the y-axis.

For the single Au rod layer (left-hand column), the y-polarized light only excites the resonance along the principal axis of the rod, which is located at a lower energy than the corresponding for the short axis (only excited using x-polarized light). Therefore, the m_{12} element has a sigmoidal spectral shape, with a negative dip centered at the position of the long axis resonance of the rod and a positive peak at the position of the short axis resonance. On the other hand, light polarized along x' or y' axes excites, in equal footing, long and short axes resonances and, as a consequence, the m_{13} values for all the wavelengths are zero. The same occurs for the circular differential extinction value, m_{14} .

A completely different behavior is observed for the rod dimers at 45 and -45 degrees (center and right-hand column). First, m_{12} is very similar for both cases, with a sigmoidal shape resembling that obtained for the individual Au rod, but less pronounced. Even though the bottom rod in the dimers still dominates the linear dichroic response of the system, the presence of the $\pm 45^\circ$ top rod, modifies it, due to both the excitation of its characteristic resonances for y - and x -polarized light, and very likely to interactions with the bottom rod. The m_{12} spectra have the same sign for both dimers, because the rotation of the upper Au rod from 45° to -45° does not alter the symmetry of the system with respect to the X and Y axis. On the other hand, the presence of the upper rod at $\pm 45^\circ$ leads now to a non-zero m_{13} , and to a change in sign in m_{13} due to the change of relative orientation of the top rod: for the dimer at 45° , the x' -polarized light excites the longitudinal mode of the top rod, and partly both longitudinal and transverse modes of the bottom rod, while y' -polarized light excites the transverse mode of the top rod and again partly both longitudinal and transverse modes of the bottom rod. However, for -45° y' - and x' -polarized light excite the modes corresponding to x' - and y' -polarization for 45° . Finally, the circular differential extinction, m_{14} , is also non-zero for these two dimers, due to their twisted structure, and the change in sign is due to the change in sign of the twist.

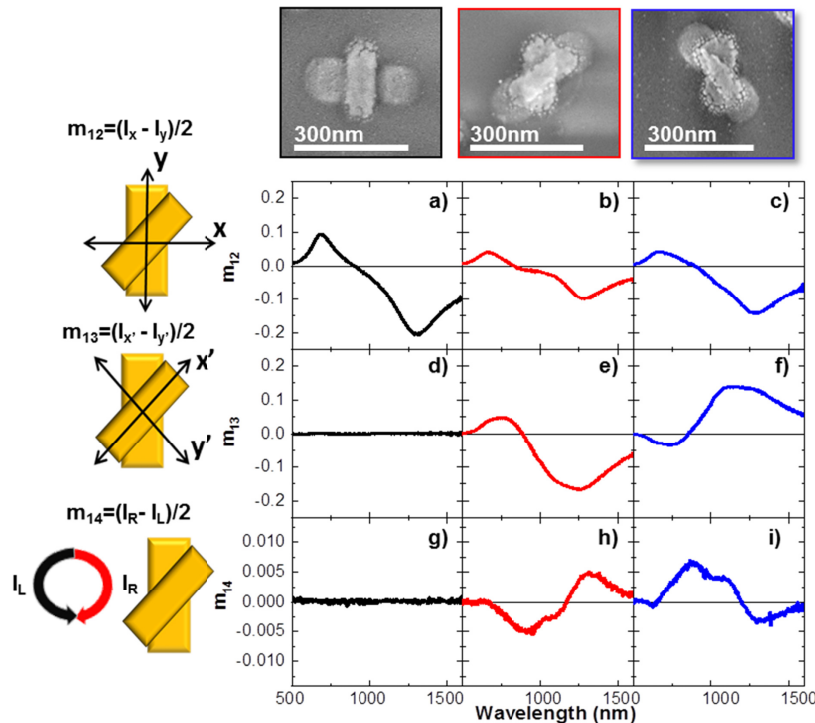


Fig. 2. Definition of the MME considered in this work and their spectral evolution for the different fabricated metasurfaces. Upper part: SEM images of the fabricated metastructures. Left hand side: schema of the configuration of the axes that define the MME shown. Figures 2(a)-2(c) Linear dichroism, m_{12} , is presented for single rod with pillars, rod dimers placed at 45° and rod dimers placed at -45° respectively. Figures 2(d)-2(f) Linear dichroism at 45° , m_{13} . Figures 2(g)-2(i) Circular differential extinction, m_{14} .

In short, the presence of the top rod induces a breaking down of the optical symmetry of the system, leading to additional linear and circular dichroism signals, whose sign depend on the relative alignment between top and bottom rods. Now, the CDE obtained in this system has contributions from both its optical anisotropy (OA), which is a linear combination of optical anisotropies such as linear dichroism and linear birefringence; and intrinsic circular

dichroism (CD_{in}). It is known that, in complex systems with small anisotropies where these two effects (optical anisotropy and intrinsic circular dichroism) coexist, it is possible to separate their contributions to the CDE by carrying out forward and backward experimental measurements, since these two magnitudes behave differently for forward and backward illumination [26,33]. The experimentally measured circular differential extinction can be decomposed in the intrinsic circular dichroism and optical anisotropy components ($CDE = CD_{in} + OA$) where

$$\begin{aligned} CD_{in} &= \left(\frac{m_{14}^F + m_{14}^B}{2} \right) \\ OA &= \left(\frac{m_{14}^F - m_{14}^B}{2} \right) \end{aligned} \quad (1)$$

It is worth noticing that the Eq. (1) is a valid approximation in the range of values of CDE that we are studying. The real values of the CDE can be extracted from the differential Mueller matrix elements [31,35–37]. It should be mentioned that the sources of the optical anisotropy are the preferential in plane ordering of the structures in the array configuration, as well as effects to the overlapping dimer. Therefore, it is possible to apply this methodology thanks to the correlated orientation of all the rods dimers between each other provided by the specific fabrication technique. This would not be possible in systems presenting a random orientation of rod dimers, such as those obtained by chemical methods, where the anisotropic contribution to the circular differential extinction cancels out [10].

In the left column of Fig. 3 we present the spectral dependence of m_{14} for forward and backward illumination for both types of dimers. As it can be observed, the forward and backward spectra of these layers are different, highlighting the presence of the two contributions. On the other hand, comparing the spectra of the two samples they are, both for forward and backward illumination, mirror images of each other (Figs. 3(a) and 3(d)), due to their opposite twist sign. As mentioned before, with this kind of measurements, the two contributions (optical anisotropy and intrinsic circular dichroism) to the circular differential extinction can be obtained, and the results are shown in Figs. 3(b) and 3(e) and in Figs. 3(c) and 3(f). As it can be observed, the spectral shape of the two contributions is different: the intrinsic circular dichroism contribution (CD_{in}) has a sigmoidal like shape, whose sign depend on the relative arrangement of the dimers, whereas the optical anisotropy contribution (OA) consists of a broad peak, whose sign also depends on the twist. Minor differences on the spectral dependencies of these magnitudes for both dimers are due to the lack of perfect morphological reproducibility in the fabrication of these mirror structures.

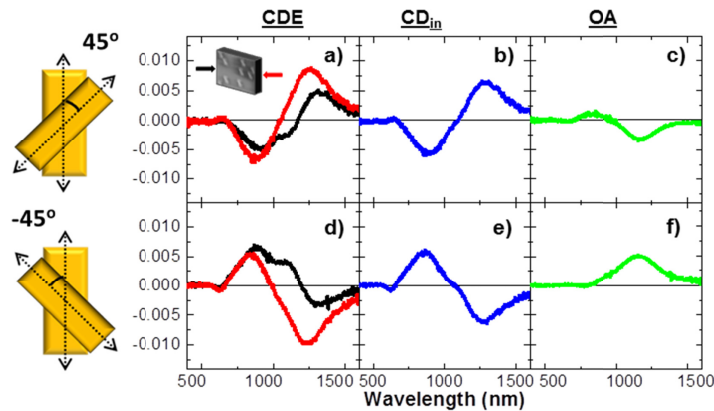


Fig. 3. The spectral dependence of the m_{14} element and its contributions for nanorod dimers at 45° and at -45° . Black (red) curves in Figs. 3(a) and 3(b) represent the spectral responses of m_{14} for the structures in backward (forward) configurations. CDE has been separated in its two contributions: intrinsic circular dichroism depicted as blue curves in Figs. 3(b) and 3(e) and the optical anisotropy depicted as green curves in Figs. 3(c) and 3(f). The insets on the left hand side shows the sketch of the measurement in forward (F) and backward (B) configurations.

Another aspect of obvious relevance in this kind of systems is the interaction between the resonant building blocks and its consequence in the optical response. To study this aspect, we have fabricated an additional rod dimer structures without dielectric CaF_2 spacer, so that the Au rods are actually in contact.

In Fig. 4, we present comparison of the dimers with spacer (already detailed in Figs. 3(a)-3(c)) with those without spacer. Regarding the CDE signal, the structures behave very differently both in terms of spectral response and under illumination direction change: while there are only subtle changes in the CDE response for the dimer with spacer, in the dimers with rods in contact a change in the illumination direction leads to almost a net sign reversal of the CDE signal. Once the two contributions to the CDE (CD_{in} and OA) are separated, the picture becomes more illustrative: while for the dimer with spacer the contribution of the intrinsic circular dichroic component dominates over the anisotropic one in terms of intensity, the reverse situation is obtained for the dimers with rods without spacer, where the optical anisotropy component dominates. It is clear that the role of the dielectric spacer to generate the 3rd dimension in the system and electrically separate the two resonant rods is crucial to endorse it with intrinsic circular dichroism. Obviously, the non-contact to contact transition between these two cases strongly affects the interactions between the rods and as a consequence to the dominance of one or the other effects.

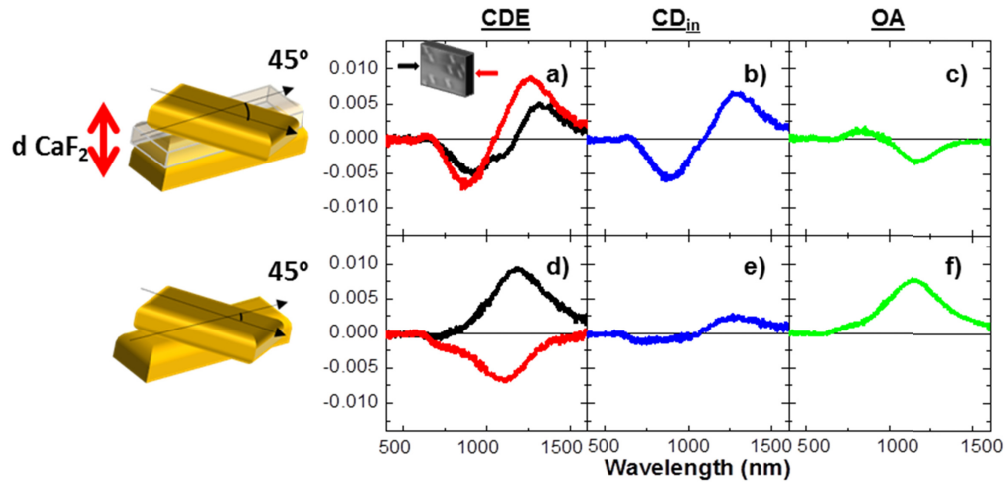


Fig. 4. Dependence of the circular differential extinction as a function of the dielectric spacer for gold rods at 45° . The $m_{1,4}$ in forward (F) (black lines) and backward (B) configurations (red lines) is shown in the cases of 6nm and 0nm of dielectric thickness. From the CDE signal, intrinsic circular dichroism (blue lines) and optical anisotropy (green lines) are extracted.

In order to shed more light into this issue, we present a theoretical modeling of the ellipsometric response for the nanorods arranged in the shape of the 45° system. To that end we have used a finite-difference time domain (FDTD) method, which takes into account all (short and long range) electromagnetic interactions between the rods [38]. The specific dimensions of the dimers are $12 \times 95 \times 235 \text{ nm}$ for the bottom rod and $12 \times 75 \times 220 \text{ nm}$ for the top rod. The lattice constant is $500 \times 500 \text{ nm}$, and we made sure that any possible effects due to the lattice (e.g. diffraction modes) are minimal. The dielectric permittivity of glass (SiO_2) has been obtained from references [39,40] and, for the sake of performance, the dielectric permittivity of gold has been modeled using a Drude-type formula:

$$\epsilon = \epsilon_\infty - \left[\frac{\omega_p^2}{(2\pi\omega)(\gamma_c + 2\pi\omega)} \right], \text{ where } \epsilon_\infty = 5.9752, \gamma_c = 3.4629610^{14} \text{ rad s}^{-1} \text{ and } \omega_p = 1.1449510^{16} \text{ rad s}^{-1}.$$

These parameters lead to a very good agreement in the position and broadening of the long axis resonance for the single rods.

To mimic the experimental case and gradually modify inter-rod interactions, in Fig. 5 we present simulations where the distance between the two constituting bars is varied from 6nm edge-to-edge, down to a complete overlap of the two bars. In this extreme case of fully overlapping bars, the system is planar and geometry considerations advise to expect a mostly vanishing intrinsic CD contribution. Thus, the signal should go from a CDE dominated by the CD_{in} contribution, through a gradual overall decrease of the CD_{in} [20,21].

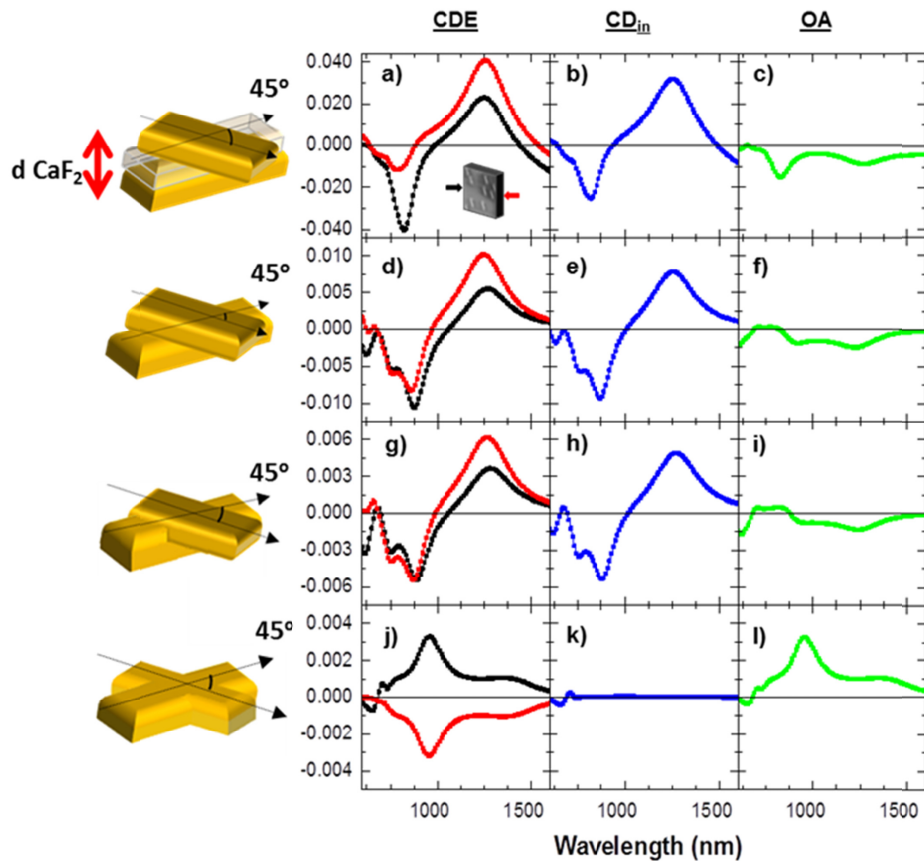


Fig. 5. Spectral dependence of the simulated MME for a rod dimer at 45° , where the evolution from a CDE dominated by the intrinsic circular dichroism contribution to a CDE where optical anisotropy governs the signal is clearly shown. Figures 5(a)–5(c) CDE, CD_{in} and OA respectively, for a 6nm spacer between the bars. Figures 5(d)–5(f) The same for touching dimers (no spacer). Figures 5(g)–5(i) Top bar halfway embedded into the bottom bar. Figures 5(j)–5(l) Fully overlapping rods, leading to a planar structure.

As it can be seen in Fig. 5, the overall quantitative reduction of the CDE as the distance between the dimers decreases is apparent, to end with an almost zero intrinsic CD signal. Once decomposed into the two contributions, the response of the CD_{in} retains its spectral dependence as long as the structure is non-planar, vanishing for the last considered case, where both Au rods are actually co-planar. On the other hand, the optical anisotropy component also decreases gradually as the third dimension is lost, presenting also an abrupt change in spectral dependence for the pure co-planar case. In the planar case, the coupling effects between the nanorods modify their responses and generate changes in the sign of the spectral response [41]. The comparison with experiments is in line with the dimer with 6 nm spacer, reproducing both the spectral dependence of the CD_{in} and optical anisotropy components, and the dominance of the first one over the second. Qualitatively, the experimental results for the dimer with rods in contact are better reproduced by the theoretical pure co-planar structure, with a clear dominance of the optical anisotropy component, good spectral dependence correlation also with the global CDE, and a minor contribution of the circular dichroic response. In view of the true morphological nature of the fabricated structures, the obtained theoretical results are satisfactory, since truly reproducing all the

existing morphological details is a great challenge. For example, it is worth noticing that, since in the modeling all interfaces are crisp and defect free, the CD_{in} keeps governing the CDE down close to the planar case. In the experimental case the spacer free system already shows an almost vanishing the intrinsic CD contribution, which we attribute to the natural fabrication constrains, such as porosity, misalignments (especially in the height of the auxiliary pillars) that largely affects the CD_{in} and tends to increase the optical anisotropy.

4. Conclusions

We have fabricated Au nanorod dimers helically stacked with different relative orientations and separation between them using a single deposition run technique. We have addressed the dependence of their linear and circular dichroism performing a careful analysis of the Mueller Matrix Elements obtained from both experimental measurements and dedicated FDTD numerical simulations. We have shown that there is a nearly proportional increase of the intrinsic circular dichroic contribution, and a dramatic change of the optical anisotropic part when departing from the planar situation. These findings highlight that the contributions to circular differential extinction can be controlled by carefully acting on the morphology of the sample.

Funding

Spanish MINECO (MAT2014-58860-P, MAT2017-84009-R); Spanish MINECO and EU (FEDER, FSE) (CSIC13-4E-1794); CM and EU (FEDER, FSE) (S2013/ICE-2822 (Space-Tec)).

Acknowledgment

We acknowledge the support from the Spanish MINECO through the projects MAT2014-58860-P and MAT2017-84009-R. We acknowledge the service from the X-SEM Laboratory at IMN, and funding from MINECO under project CSIC13-4E-1794 with support from EU (FEDER, FSE). We acknowledge the service from MiNa Laboratory at IMN, and funding from CM under project S2013/ICE-2822 (Space-Tec) with support from EU (FEDER, FSE).

Disclosures

The authors declare that there are no conflicts of interest related to this article.

References

1. L. Vigderman, B. P. Khanal, and E. R. Zubarev, "Functional gold nanorods: synthesis, self-assembly, and sensing applications," *Adv. Mater.* **24**(36), 4811–4841 (2012).
2. G. Armelles, A. Cebollada, F. García, A. García-Martín, and N. de Sousa, "Far- and Near-Field Broad-Band Magneto-Optical Functionalities Using Magnetoplasmonic Nanorods," *ACS Photonics* **3**(12), 2427–2433 (2016).
3. A. F. Najafabadi and T. Pakizeh, "Analytical Chiroptics of 2D and 3D Nanoantennas," *ACS Photonics* **4**(6), 1447–1452 (2017).
4. A. F. Najafabadi and T. Pakizeh, "Optical absorbing origin of chiroptical activity in planar plasmonic metasurfaces," *Sci. Rep.* **7**(1), 10251 (2017).
5. E. J. Smythe, E. Cubukcu, and F. Capasso, "Optical properties of surface plasmon resonances of coupled metallic nanorods," *Opt. Express* **15**(12), 7439–7447 (2007).
6. C. de Dios, H. Yu Feng, F. García, A. Cebollada, and G. Armelles, "Analysis of the Optical Properties of Chiral Au Nanorod Stacks," *Plasmonics* **13**(6), 2061–2066 (2018).
7. Z. Li, W. Liu, H. Cheng, S. Chen, and J. Tian, "Spin-Selective Transmission and Devisable Chirality in Two-Layer Metasurfaces," *Sci. Rep.* **7**(1), 8204 (2017).
8. R. Taubert, R. Ameling, T. Weiss, A. Christ, and H. Giessen, "From near-field to far-field coupling in the third dimension: retarded interaction of particle plasmons," *Nano Lett.* **11**(10), 4421–4424 (2011).
9. M. Hentschel, M. Schäferling, X. Duan, H. Giessen, and N. Liu, "Chiral plasmonics," *Sci. Adv.* **3**(5), e1602735 (2017).
10. S. Fasold, S. Linß, T. Kawde, M. Falkner, M. Decker, T. Pertsch, and I. Staude, "Disorder-Enabled Pure Chirality in Bilayer Plasmonic Metasurfaces," *ACS Photonics* **5**(5), 1773–1778 (2018).
11. X. Yin, M. Schäferling, B. Metzger, and H. Giessen, "Interpreting chiral nanophotonic spectra: the plasmonic

- Born-Kuhn model,” *Nano Lett.* **13**(12), 6238–6243 (2013).
12. L.-Y. Wang, K. W. Smith, S. Dominguez-Medina, N. Moody, J. M. Olson, H. Zhang, W.-S. Chang, N. Kotov, and S. Link, “Circular Differential Scattering of Single Chiral Self-Assembled Gold Nanorod Dimers,” *ACS Photonics* **2**(11), 1602–1610 (2015).
 13. A. Guerrero-Martínez, J. L. Alonso-Gómez, B. Auguie, M. M. Cid, and L. M. Liz-Marzán, “From individual to collective chirality in metal nanoparticles,” *Nano Today* **6**(4), 381–400 (2011).
 14. A. Kuzyk, R. Jungmann, G. P. Acuna, and N. Liu, “DNA Origami Route for Nanophotonics,” *ACS Photonics* **5**(4), 1151–1163 (2018).
 15. A. Azizi, B. Ranjbar, T. T. Moghadam, and Z. Bagheri, “Plasmonic circular dichroism study of DNA–gold nanoparticles bioconjugates,” *Plasmonics* **9**(2), 273–281 (2014).
 16. W. Ma, H. Kuang, L. Wang, L. Xu, W.-S. Chang, H. Zhang, M. Sun, Y. Zhu, Y. Zhao, L. Liu, C. Xu, S. Link, and N. A. Kotov, “Chiral plasmonics of self-assembled nanorod dimers,” *Sci. Rep.* **3**(1), 1934 (2013).
 17. H. Fredriksson, Y. Alaverdyan, A. Dmitriev, C. Langhammer, D. S. Sutherland, M. Zäch, and B. Kasemo, “Hole–Mask Colloidal Lithography,” *Adv. Mater.* **19**(23), 4297–4302 (2007).
 18. D. Meneses-Rodríguez, E. Ferreira-Vila, P. Prieto, J. Anguita, M. U. González, J. M. García-Martín, A. Cebollada, A. García-Martín, and G. Armelles, “Probing the electromagnetic field distribution within a metallic nanodisk,” *Small* **7**(23), 3317–3323 (2011).
 19. J. C. Bantñi, D. Meneses-Rodríguez, F. García, M. U. González, A. García-Martín, A. Cebollada, and G. Armelles, “High magneto-optical activity and low optical losses in metal-dielectric Au/Co/Au-SiO₂ magnetoplasmonic nanodisks,” *Adv. Mater.* **24**(10), OP36–OP41 (2012).
 20. G. Armelles, A. Cebollada, A. García-Martín, M. U. González, F. García, D. Meneses-Rodríguez, N. de Sousa, and L. S. Froufe-Pérez, “Mimicking electromagnetically induced transparency in the magneto-optical activity of magnetoplasmonic nanoresonators,” *Opt. Express* **21**(22), 27356–27370 (2013).
 21. N. De Sousa, L. S. Froufe-Pérez, G. Armelles, A. Cebollada, M. U. González, F. García, D. Meneses-Rodríguez, and A. García-Martín, “Interaction effects on the magneto-optical response of magnetoplasmonic dimers,” *Phys. Rev. B Condens. Matter Mater. Phys.* **89**(20), 205419 (2014).
 22. C. A. Herreño-Fierro, E. J. Patiño, G. Armelles, and A. Cebollada, “Surface sensitivity of optical and magneto-optical and ellipsometric properties in magnetoplasmonic nanodisks,” *Appl. Phys. Lett.* **108**(2), 021109 (2016).
 23. H. Y. Feng, F. Luo, R. Kekesi, D. Granados, J. M. García, A. García-Martín, G. Armelles, and A. Cebollada, “Magnetoplasmonic nanorings as novel architectures with tunable magneto-optical activity in wide wavelength ranges,” *Adv. Opt. Mater.* **2**(7), 612–617 (2014).
 24. H. Y. Feng, D. Meneses-Rodríguez, G. Armelles, and A. Cebollada, “From disk to ring: Aspect ratio control of the magnetoplasmonic response in Au/Co/Au nanostructures fabricated by hole-mask colloidal lithography,” *Appl. Phys. Lett.* **106**(8), 083105 (2015).
 25. H. Y. Feng, F. Luo, R. Arenal, L. Henrard, F. García, G. Armelles, and A. Cebollada, “Active magnetoplasmonic split-ring/ring nanoantennas,” *Nanoscale* **9**(1), 37–44 (2017).
 26. H. Y. Feng, C. de Dios, F. García, A. Cebollada, and G. Armelles, “Analysis and magnetic modulation of chiro-optical properties in anisotropic chiral and magneto-chiral plasmonic systems,” *Opt. Express* **25**(25), 31045–31055 (2017).
 27. S. Syrenova, C. Wadell, and C. Langhammer, “Shrinking-hole colloidal lithography: self-aligned nanofabrication of complex plasmonic nanoantennas,” *Nano Lett.* **14**(5), 2655–2663 (2014).
 28. H. Fujiwara, *Spectroscopic Ellipsometry: Principles and Applications*, 1st ed. (Wiley, 2007).
 29. C. Menzel, C. Rockstuhl, and F. Lederer, “Advanced Jones calculus for the classification of periodic metamaterials,” *Phys. Rev. A* **82**(5), 053811 (2010).
 30. G. Armelles, A. Cebollada, H. Y. Feng, A. García-Martín, D. Meneses-Rodríguez, J. Zhao, and H. Giessen, “Interaction Effects between Magnetic and Chiral Building Blocks: A New Route for Tunable Magneto-chiral Plasmonic Structures,” *ACS Photonics* **2**(9), 1272–1277 (2015).
 31. M. Schulz, J. Zablocki, O. S. Abdullaeva, S. Brück, F. Balzer, A. Lützen, O. Arteaga, and M. Schiek, “Giant intrinsic circular dichroism of prolinol-derived squaraine thin films,” *Nat. Commun.* **9**(1), 2413 (2018).
 32. A. Harland Tompkins Eugene, Irene, *Handbook of Ellipsometry*, 1st ed. (2005).
 33. O. Arteaga, J. Sancho-Parramon, S. Nichols, B. M. Maoz, A. Canillas, S. Bosch, G. Markovich, and B. Kahr, “Relation between 2D/3D chirality and the appearance of chiroptical effects in real nanostructures,” *Opt. Express* **24**(3), 2242–2252 (2016).
 34. O. Arteaga and A. Canillas, “Pseudopolar decomposition of the Jones and Mueller-Jones exponential polarization matrices,” *J. Opt. Soc. Am. A* **26**(4), 783–793 (2009).
 35. O. Arteaga and B. Kahr, “Characterization of homogenous depolarizing media based on Mueller matrix differential decomposition,” *Opt. Lett.* **38**(7), 1134–1136 (2013).
 36. H. Arwin, A. Mendoza-Galván, R. Magnusson, A. Andersson, J. Landin, K. Järrendahl, E. García-Caurel, and R. Ossikovski, “Structural circular birefringence and dichroism quantified by differential decomposition of spectroscopic transmission Mueller matrices from *Cetonia aurata*,” *Opt. Lett.* **41**(14), 3293–3296 (2016).
 37. N. Agarwal, J. Yoon, E. García-Caurel, T. Novikova, J.-C. Vanel, A. Pierangelo, A. Bykov, A. Popov, I. Meglinski, and R. Ossikovski, “Spatial evolution of depolarization in homogeneous turbid media within the differential Mueller matrix formalism,” *Opt. Lett.* **40**(23), 5634–5637 (2015).
 38. Lumerical Inc, “<https://www.lumerical.com/tcad-products/fdtd/>,” (n.d.).
 39. P. B. Johnson and R. W. Christy, “Optical constants of the noble metals,” *Phys. Rev. B* **6**(12), 4370–4379

- (1972).
40. F. M. Ratcliffe, "Absence of morphine glucuronidation in the human lung," *Eur. J. Clin. Pharmacol.* **37**(5), 537–538 (1989).
 41. E. Kuntman, M. A. Kuntman, J. Sancho-Parramon, and O. Arteaga, "Formalism of optical coherence and polarization based on material media states," *Phys. Rev. A (Coll. Park)* **95**(6), 063819 (2017).